# Fluorescence-Encoded Infrared Vibrational Spectroscopy with Single-Molecule Sensitivity

Lukas Whaley-Mayda, Abhirup Guha, Samuel B. Penwell, and Andrei Tokmakoff*

Department of Chemistry, James Franck Institute, and Institute for Biophysical Dynamics, The University of Chicago, Chicago, Illinois 60637, United States

*Supporting Information Placeholder*

**ABSTRACT:** Single-molecule methods have revolutionized molecular science, but techniques possessing the structural sensitivity required for chemical problems—e.g. vibrational spectroscopy—remain difficult to apply in solution. Here, we describe how coupling infrared-vibrational absorption to a fluorescent electronic transition (fluorescence-encoded infrared (FEIR) spectroscopy) can achieve single-molecule sensitivity in solution with conventional far-field optics. Using the fluorophore Coumarin 6, we illustrate the principles by which FEIR spectroscopy measures vibrational spectra and relaxation and introduce FEIR correlation spectroscopy, a vibrational analogue of fluorescence correlation spectroscopy, to demonstrate single-molecule sensitivity. With further improvements, FEIR spectroscopy could become a powerful tool for single-molecule vibrational investigations in the solution or condensed phase.

Single-molecule (SM) spectroscopy has had a profound impact on how we describe molecular phenomena in chemistry, biology, and materials science. Studying the behavior of individuals reveals information hidden within the ensemble average, while the ability to access trajectories of a molecular observable at equilibrium provides dynamical information without the need for synchronization. Since the early pioneering experiments, fluorescence has become the most widely adapted method for SM detection, due to the bright, background-free signal coupled with sensitive single-photon detectors and modern microscopy tools.[1-5] While the capabilities of SM fluorescence have been revolutionary, its limited structural specificity often restricts its applicability for chemical problems. This shortcoming has inspired a concurrent development of SM vibrational techniques, which offer a sensitivity to chemical bonding and specific molecular contacts through the frequencies and lineshapes of vibrational bands. However, most of these methods, including surface- and tip-enhanced Raman spectroscopy (SERS and TERS), [6-9] atomic force microscopy infrared spectroscopy (AFM-IR),[10] infrared scattering-type scanning near-field optical microscopy (IR-sSNOM),[11] and scanning tunneling microscopy (STM),[12] require contact with a solid interface, probe, or nanostructure, precluding their application to solution-phase systems. This Communication presents evidence that infrared (IR) spectroscopy is possible with SM sensitivity using fluorescence encoding, providing a new strategy for SM vibrational spectroscopy compatible with chemical systems in solution.

Coupling the vibrational excitation to a fluorescent electronic transition is an attractive strategy that benefits from the experimental and technical advantages of far-field fluorescence detection, including solution-phase compatibility. Double resonance schemes that first excite vibrations via infrared absorption or stimulated Raman pumping and then up-convert the molecule to an emissive electronic excited state have existed since the 1970's to perform vibrational spectroscopy with increased detection sensitivity.[13-18] Recently, Xiong et al achieved SM detection with stimulated Raman excited fluorescence (SREF) spectroscopy, representing the first far-field SM vibrational measurement.[19] Our group has adapted an IR-pumped double resonance method, fluorescence-encoded IR (FEIR) spectroscopy, using broadband femtosecond pulses to perform ultrafast Fourier transform vibrational spectroscopy,[20-21] and recently developed a high-sensitivity experimental configuration incorporating confocal fluorescence microscopy to achieve 10-100 nM sensitivity in solution.[22] Here we build on those results to perform FEIR correlation spectroscopy, an IR-vibrational analogue of fluorescence correlation spectroscopy (FCS), demonstrating that FEIR spectroscopy can achieve SM sensitivity, i.e. where on average less than one molecule contributes to the signal at any given time.

FEIR spectroscopy operates by the double resonance scheme depicted in Figure 1a. An IR pulse or pulse-pair resonantly drives vibrations into their first excited state, after which an electronically pre-resonant visible pulse selectively brings the fluorophore to its electronic excited state. The resulting fluorescence emission intensity is therefore dependent on the excited vibrational population created by the IR field on the ground electronic state and is used as an action signal that encodes vibrational information. In practice, the weak IR-vibrational absorption cross-sections and picosecond lifetimes necessitate intense pulses with comparable or shorter durations to ensure the overall excitation process is competitive against relaxation. Furthermore, high repetition-rates benefit single-photon counting but must be balanced with the technical requirements of generating intense, ultrashort mid-IR pulses and potential heating artifacts.

FEIR measurements are performed with the experimental scheme summarized in Figure 1b.[22] We use 200-300 fs mid-IR and visible pulses derived from a 1 MHz fiber laser,[23] enabling time-resolved measurements of vibrational relaxation processes, as well as broadband excitation of multiple modes. To achieve intense excitation fields and a small probe volume, the IR and visible beams are focused into the sample with high numerical aperture (NA) optics in a counter-propagating geometry, with the smaller diffraction-limited visible focus (340 nm $1/e^2$ radius, 0.2-30 pJ pulse energy) centered within the larger IR focus (9 μm, 50 nJ). Fluorescence is collected with the same visible objective lens, passed through selective bandpass filters, and imaged onto a single-photon avalanche photodiode (SPAD) with its small active area serving as

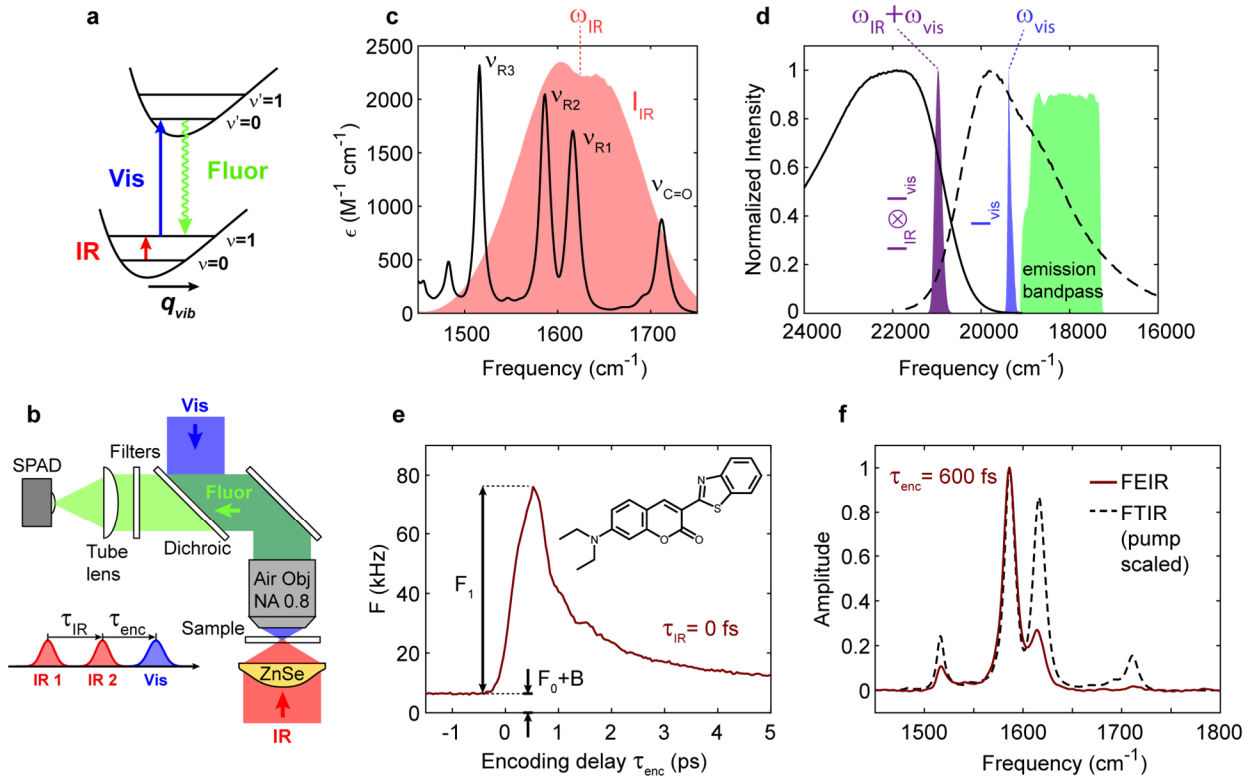


Figure 1: (a) Energy level diagram for FEIR spectroscopy. (b) Experimental schematic of the FEIR microscope and pulse sequence. (c) FTIR spectrum of C6 in acetonitrile-d3 with IR pulse spectrum. (d) Electronic absorption (solid) and fluorescence (dashed) spectra with the visible pulse spectrum, convolution of visible and IR pulse spectra (distribution of their frequency sums), and emission bandpass. (e) 1-IR-pulse FEIR data on a 30 μM C6 solution. Molecular structure of C6 is inset. (f) FEIR spectrum of the same sample at $\tau_{enc} = 600$ fs compared with the FTIR spectrum scaled by the IR pulse spectrum. Data acquisition times for (e) and (f) were <5 minutes.



a confocal aperture. A vibrational spectrum is acquired in Fourier transform mode with two IR pulses derived from an interferometer.

The quality of the double resonance condition plays a crucial role for achieving sensitive FEIR vibrational detection, demonstrated here with the fluorophore Coumarin 6 (C6) in acetonitrile-d3. Figure 1c shows that the tunable IR pulses have the spectral breadth to be resonant with the carbonyl ($\nu_{C=O}$) and three highest frequency C=C ring ($\nu_{R1\text{-}3}$) vibrations when centered at $\omega_{IR} = 1620$ cm$^{-1}$. Figure 1d shows the electronic absorption and fluorescence spectra of C6. Maximal resonance for the encoding transition is achieved when the sum of IR and visible center frequencies ($\omega_{IR} + \omega_{vis} = 20980$ cm$^{-1}$, $\lambda_{sum} = 477$ nm) falls near the peak of the electronic absorption band. However, the visible pulse (fixed center frequency $\omega_{vis} = 19360$ cm$^{-1}$, $\lambda_{vis} = 517$ nm) alone directly excites the red tail of the band, creating undesirable background fluorescence. The resonance condition shown in Figure 1d is likely a nearly ideal compromise between large FEIR resonance and low one-photon background, but could be further optimized with a tunable visible pulse.

Figure 1e shows the total fluorescence count rate from a 30 μM C6 solution as a function of the IR-visible pulse time delay, or encoding delay $\tau_{enc}$, for excitation with a single IR pulse. The baseline apparent for $\tau_{enc} < 0$ is the sum of the aforementioned one-photon excited fluorescence $F_0$ and non-molecular background $B$, including solvent Raman scattering, impurity and optics fluorescence, and detector dark-counts. After a nearly pulse-limited rise to a maximum labeled $F_1$, the FEIR signal decays away, tracking the vibrations' population relaxation kinetics. The FEIR vibrational spectrum at $\tau_{enc} = 600$ fs, corresponding to the signal maximum in Figure 1e, is shown in Figure 1f overlaid on the FTIR linear absorption spectrum scaled by the spectrum of the IR pulse. The FEIR spectrum is free of background due to the Fourier transform acquisition modality. Recording FEIR spectra as a function of $\tau_{enc}$ would resolve the decay transient by vibrational mode. Differences in relative peak amplitudes between the FEIR and conventional IR spectra are due to the contribution of vibrational-electronic coupling in the former, which controls the strength of the electronic encoding transition. Specifically, the factor of 5 difference in FEIR intensity between the similarly IR-intense $\nu_{R2}$ and $\nu_{R1}$ modes at 1586 and 1616 cm$^{-1}$ as well as the nearly absent $\nu_{C=O}$ band at 1712

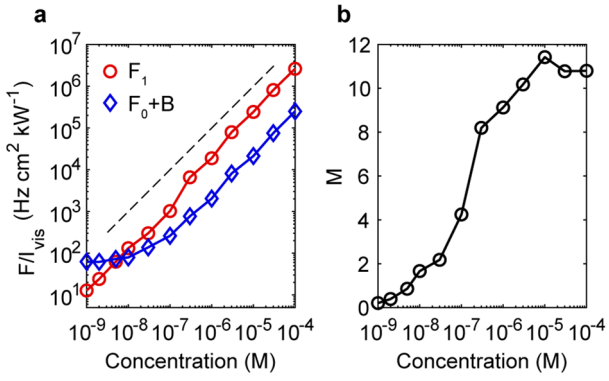


Figure 2: (a) C6 concentration dependence of $F_1/I_{vis}$ (red circles) and $(F_0 + B)/I_{vis}$ (blue diamonds). Dashed line shows a linear dependence for reference. (b) Modulation ratios $M$ corresponding to panel (a).

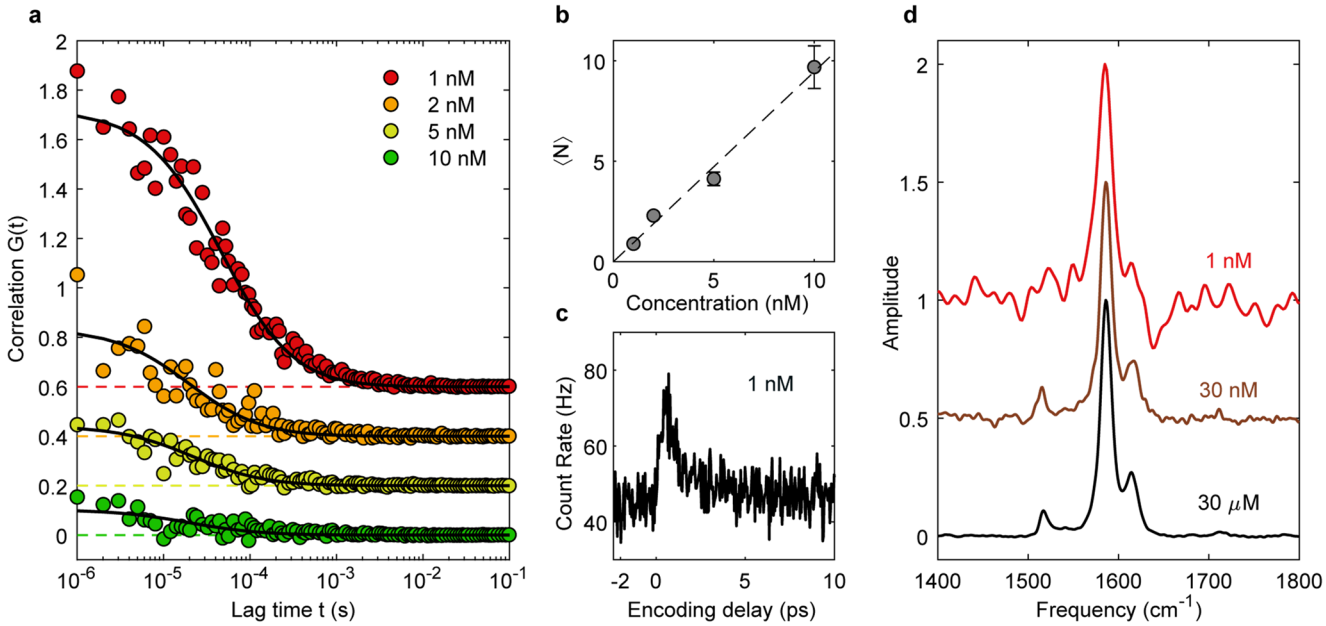


Figure 3: (a) FEIR correlation functions from C6 solutions at 1, 2, 5, and 10 nM (offset for clarity with zero-levels indicated by dashed lines). Fits are shown by black lines. (b) $\langle N \rangle = G(0)^{-1}$ from the fits in (a) as a function of concentration, with the linear trend shown by a dashed line. (c) 1-IR-pulse FEIR transient from the 1 nM solution. (d) FEIR spectra at 1 nM, 30 nM, and 30 μM (offset for clarity). The visible pulse energy was 25 pJ for (a), (b), and the 1 nM spectrum in (d), and 12 pJ in (c). Acquisition times were 60 minutes in (a), and 30 minutes for (c) and 1 and 30 nM data in (d).

cm$^{-1}$ are well described by these vibrations' respective Huang-Rhys factors.[24]

The ultimate detection sensitivity of an FEIR measurement hinges upon the ability to resolve the FEIR signal $F_1$ against the background $F_0 + B$, quantified by the modulation ratio $M = F_1/(F_0 + B)$. Maximizing $M$ therefore requires simultaneously optimizing the brightness of molecular fluorescence $F_1 + F_0$ against $B$, as well as $F_1$ against $F_0$—a non-trivial problem strongly influenced by the double resonance condition discussed above.

Figure 2a shows the concentration dependence of the maximum $F_1$ signal and background level $F_0 + B$ for C6, scaled by the visible excitation intensity $I_{vis}$. While the FEIR signal is roughly linear in concentration across the entire range, the background levels off to a concentration-independent value in the nM regime. This constant level represents $I_{vis}$ dependent contributions to $B$, likely solvent Raman scattering or fluorescence from impurities and optics. Correspondingly, $M$ (Figure 2b) falls by nearly two orders of magnitude from its $B$-free value of ~11 in the μM range. Using time-correlated single-photon counting (TCSPC), prompt scattering background can be suppressed by time-gating data acquisition for photon arrivals between 1-15 ns after the encoding pulse (Supporting Information Section 3). At the lowest 1 nM concentration investigated, this results in a 4-fold reduction in background at the expense of 30% loss in FEIR signal, improving $M$ from 0.2 to 0.6.

As a demonstration of SM sensitivity, we perform fluctuation correlation spectroscopy with the FEIR signal to count the average number of molecules that contribute at a given time. In analogy to FCS,[25] we measure the correlation function $G(t) = \langle \delta F(0) \delta F(t) \rangle / \langle F \rangle^2$, where $F(t)$ is the real-time photon stream from an FEIR measurement with optical delays fixed at the maximum signal level ($\tau_{IR} = 0$ fs, $\tau_{enc} = 600$ fs for C6). Like a conventional FCS experiment, diffusion of molecules through the probe volume produces spontaneous fluctuations in $F(t)$, causing $G(t)$ to decay with the characteristic timescale of these transits with early-time amplitude given by the inverse of the average molecule number $G(0) = \langle N \rangle^{-1}$.

Figure 3a shows FEIR correlation functions from C6 solutions at 1, 2, 5, and 10 nM along with fits to a standard diffusion model assuming an 3D-ellipsoidal Gaussian probe volume (Supporting Information Section 5). As demonstrated in Figure 3b, $\langle N \rangle$ extracted from the fits depends linearly on concentration, with roughly one molecule at 1 nM. The dependence of $G(0)$ on the starting edge of the time-gate used for the 1 nM correlation function reaches ~1.5 for gates >2 ns (Figure S4), and we take the corresponding value of $\langle N \rangle = 0.65$ as our estimate of the average molecule number. The $F_1$ count rate per molecule (un-gated) is 110 Hz, which, accounting for the 0.63 fluorescence quantum yield and estimated 1% instrument collection efficiency, corresponds to a 2% overall excitation efficiency per pulse sequence.[26] Figures 3c and 3d show the FEIR decay transient and spectrum recorded from the 1 nM solution, demonstrating that the vibrational relaxation and frequency of the brightest ring mode $\nu_{R2}$ can still be reliably measured at this level.

We note that the FEIR experiments shown here are fundamentally ensemble measurements, even if $\langle N \rangle < 1$. To clarify this point we highlight the distinction, commonly invoked in the context of FCS within SM fluorescence,[27] between SM detection—exclusively observing a particular individual for an extended period—and SM sensitivity—the ability to measure signals and resolve changes caused by individuals. Our proof-of-principle demonstration of FEIR correlation spectroscopy (FEIR-CS) establishes SM sensitivity in that it requires the observation of correlated bursts of FEIR photons from individual molecules. Furthermore, our determination that ensemble FEIR vibrational spectra and relaxation transients can be measured 'one molecule at a time' is an encouraging sensitivity milestone along the path toward realizing true SM observation. Many opportunities to optimize this technique are available, including tunable visible excitation, increasing collection efficiency, and—crucially—higher repetition-rates, and we note that the pros and cons established by comparison to the related

SM SREF spectroscopy developed by Min and co-workers—featuring tunable, frequency-domain stimulated Raman excitation—will offer important insight.[18-19, 28]

As an intermediate step toward SM spectroscopy, FEIR-CS has potential as a powerful vibrational probe of chemical processes in solution, just as FCS often plays an auxiliary role to SM fluorescence experiments. While vibrational analogues of FCS using Raman scattering have been implemented previously, to our knowledge FEIR-CS is the first to be sensitive enough for use with single molecules.[29-31] Changes in vibrational frequencies due to chemical interconversion or specific molecular interactions in an equilibrium state could be sensed as FEIR signal fluctuations and monitored via the correlation function. Fourier transform excitation with the IR pulse-pair suggests the possibility of more sophisticated frequency-resolved FEIR-CS experiments, similar in concept to photon correlation Fourier spectroscopy,[32-33] that could track microsecond spectral diffusion processes.

In conclusion, we have demonstrated that FEIR vibrational spectroscopy can be performed with SM sensitivity. Careful optimization of the resonance condition is crucial for achieving sufficient signal brightness, while time-resolved photon detection can significantly reduce background levels. We demonstrated proof-of-concept FEIR-CS, which has the potential for development as a vibrational analogue of FCS for studying kinetics of chemical systems in solution with enhanced structural sensitivity. With improvements to the methods reported here, we believe true SM vibrational detection using FEIR spectroscopy is within reach.

## ASSOCIATED CONTENT

### Supporting Information

The Supporting Information is available free of charge on the ACS Publications website.

Experimental methods and further details of data acquisition and processing (PDF).

## AUTHOR INFORMATION


### Corresponding Author

Andrei Tokmakoff - Department of Chemistry, James Franck Institute, and Institute for Biophysical Dynamics, The University of Chicago, Chicago, Illinois 60637, United States; Email: tokmakoff@uchicago.edu

### Authors

Lukas Whaley-Mayda - Department of Chemistry, James Franck Institute, and Institute for Biophysical Dynamics, The University of Chicago, Chicago, Illinois 60637, United States

Abhirup Guha - Department of Chemistry, James Franck Institute, and Institute for Biophysical Dynamics, The University of Chicago, Chicago, Illinois 60637, United States

Samuel B. Penwell - Department of Chemistry, James Franck Institute, and Institute for Biophysical Dynamics, The University of Chicago, Chicago, Illinois 60637, United States


### Notes

The authors declare no competing financial interests.

## ACKNOWLEDGMENT


This work was supported by a grant from the National Science Foundation (CHE-1856684).


## REFERENCES


(1) Moerner, W. E.; Kador, L., Optical detection and spectroscopy of single molecules in a solid. *Physical Review Letters* **1989,** *62*, 2535-2538. DOI:10.1103/PhysRevLett.62.2535

(2) Orrit, M.; Bernard, J., Single pentacene molecules detected by fluorescence excitation in a p-terphenyl crystal. *Physical Review Letters* **1990,** *65*, 2716-2719. DOI:10.1103/PhysRevLett.65.2716

(3) Ambrose, W. P.; Moerner, W. E., Fluorescence spectroscopy and spectral diffusion of single impurity molecules in a crystal. *Nature* **1991,** *349*, 225-227. DOI:10.1038/349225a0

(4) Xie, X. S.; Dunn, R. C., Probing single molecule dynamics. *Science* **1994,** *265*, 361-364. DOI:10.1126/science.265.5170.361

(5) Moerner, W. E.; Shechtman, Y.; Wang, Q., Single-molecule spectroscopy and imaging over the decades. *Faraday Discussions* **2015,** *184*, 9-36. DOI:10.1039/c5fd00149h

(6) Kneipp, K.; Wang, Y.; Kneipp, H.; Perelman, L. T.; Itzkan, I.; Dasari, R. R.; Feld, M. S., Single molecule detection using surface-enhanced raman scattering (SERS). *Physical Review Letters* **1997,** *78*, 1667-1670. DOI:10.1103/PhysRevLett.78.1667

(7) Haran, G., Single-molecule raman spectroscopy: A probe of surface dynamics and plasmonic fields. *Accounts of Chemical Research* **2010,** *43*, 1135-1143. DOI:10.1021/ar100031v

(8) Dey, S.; Apkarian, V. A.; Potma, E. O.; Fishman, D. A.; Banik, M.; Yampolsky, S.; Hulkko, E., Seeing a Single Molecule Vibrate through Time-Resolved Coherent Anti-Stokes Raman Scattering. *Nature Photonics* **2014,** *8*, 650-656. DOI:10.1038/nphoton.2014.143

(9) Zrimsek, A. B.; Chiang, N.; Mattei, M.; Zaleski, S.; McAnally, M. O.; Chapman, C. T.; Henry, A. I.; Schatz, G. C.; Van Duyne, R. P., Single-Molecule Chemistry with Surface- and Tip-Enhanced Raman Spectroscopy. *Chemical Reviews* **2017,** *117*, 7583-7613. DOI:10.1021/acs.chemrev.6b00552

(10) Ruggeri, F. S.; Mannini, B.; Schmid, R.; Vendruscolo, M.; Knowles, T. P. J., Single molecule secondary structure determination of proteins through infrared absorption nanospectroscopy. *Nature Communications* **2020,** *11*, 1-9. DOI:10.1038/s41467-020-16728-1

(11) Xu, X. G.; Rang, M.; Craig, I. M.; Raschke, M. B., Pushing the sample-size limit of infrared vibrational nanospectroscopy: From monolayer toward single molecule sensitivity. *Journal of Physical Chemistry Letters* **2012,** *3*, 1836-1841. DOI:10.1021/jz300463d

(12) Stipe, B. C.; Rezaei, M. A.; Ho, W., Single-molecule vibrational spectroscopy and microscopy. *Science* **1998,** *280*, 1732-1735. DOI:10.1126/science.280.5370.1732

(13) Laubereau, A.; Seilmeier, A.; Kaiser, W., A New Technique to Measure Ultrashort Vibrational Relaxation Times in Liquid Systems. *Chem. Phys. Let.* **1975,** *36*, 232-237.

(14) Wright, J. C., Double Resonance Excitation of Fluorescence in the Condensed Phase—An Alternative to Infrared, Raman, and Fluorescence Spectroscopy. *Applied Spectroscopy, Vol. 34, Issue 2, pp. 151-157* **1980,** *34*, 151-157.

(15) Nguyen, D. C.; Wright, J. C.; Lee, S. H., Double Resonance Excitation of Fluorescence by Stimulated Raman Scattering. *Applied Spectroscopy, Vol. 37, Issue 5, pp. 472-474* **1983,** *37*, 472-474.

(16) Hübner, H. J.; Wörner, M.; Kaiser, W.; Seilmeier, A., Subpicosecond vibrational relaxation of skeletal modes in polyatomic molecules. *Chemical Physics Letters* **1991,** *182*, 315-320. DOI:10.1016/0009-2614(91)80221-I

(17) Winterhalder, M. J.; Zumbusch, a.; Lippitz, M.; Orrit, M., Toward far-field vibrational spectroscopy of single molecules at room temperature. *The journal of physical chemistry. B* **2011,** *115*, 5425-30. DOI:10.1021/jp109652s

(18) Xiong, H.; Min, W., Combining the best of two worlds: Stimulated Raman excited fluorescence. *The Journal of Chemical Physics* **2020,** *153*, 210901-210901. DOI:10.1063/5.0030204

(19) Xiong, H.; Shi, L.; Wei, L.; Shen, Y.; Long, R.; Zhao, Z.; Min, W., Stimulated Raman excited fluorescence spectroscopy and imaging. *Nature Photonics* **2019**, 1-13. DOI:10.1038/s41566-019-0396-4

(20) Mastron, J. N.; Tokmakoff, A., Two-Photon-Excited Fluorescence-Encoded Infrared Spectroscopy. *The Journal of Physical Chemistry A* **2016,** *120*, 9178-9187. DOI:10.1021/acs.jpca.6b09158

(21) Mastron, J. N.; Tokmakoff, A., Fourier Transform Fluorescence-Encoded Infrared Spectroscopy. *Journal of Physical Chemistry A* **2018,** *122*, 554-562. DOI:10.1021/acs.jpca.7b10305

(22) Whaley-Mayda, L.; Penwell, S. B.; Tokmakoff, A., Fluorescence-Encoded Infrared Spectroscopy: Ultrafast Vibrational Spectroscopy on Small Ensembles of Molecules in Solution. *The Journal of Physical Chemistry Letters* **2019,** *10*, 1967-1972. DOI:10.1021/acs.jpclett.9b00748

(23) Penwell, S. B.; Whaley-Mayda, L.; Tokmakoff, A., Single-stage MHz mid-IR OPA using LiGaS 2 and a fiber laser pump source. *Optics Letters* **2018,** *43*, 1363-1363. DOI:10.1364/OL.43.001363
(24) Von Cosel, J.; Cerezo, J.; Kern-Michler, D.; Neumann, C.; Van Wilderen, L. J. G. W.; Bredenbeck, J.; Santoro, F.; Burghardt, I., Vibrationally resolved electronic spectra including vibrational pre-excitation: Theory and application to VIPER spectroscopy. *Journal of Chemical Physics* **2017,** *147*. DOI:10.1063/1.4999455
(25) Krichevsky, O.; Bonnet, G., Fluorescence correlation spectroscopy: the technique and its applications. *Reports on Progress in Physics* **2002,** *65*, 251-297. DOI:10.1088/0034-4885/65/2/203
(26) Jones, G.; Jackson, W. R.; Choi, C. Y.; Bergmark, W. R., Solvent effects on emission yield and lifetime for coumarin laser dyes. Requirements for a rotatory decay mechanism. *Journal of Physical Chemistry* **1985,** *89*, 294-300. DOI:10.1021/j100248a024
(27) Moerner, W. E.; Fromm, D. P., Methods of single-molecule fluorescence spectroscopy and microscopy. *Review of Scientific Instruments* **2003,** *74*, 3597-3619. DOI:10.1063/1.1589587
(28) Xiong, H.; Qian, N.; Miao, Y.; Zhao, Z.; Min, W., Stimulated Raman Excited Fluorescence Spectroscopy of Visible Dyes. *The Journal of Physical Chemistry Letters* **2019**, 3563-3570. DOI:10.1021/acs.jpclett.9b01289
(29) Schrof, W.; Klingler, J.; Rozouvan, S.; Horn, D., Raman correlation spectroscopy: A method for studying chemical composition and dynamics of disperse systems. *Physical Review E - Statistical Physics, Plasmas, Fluids, and Related Interdisciplinary Topics* **1998,** *57*, R2523-R2526. DOI:10.1103/PhysRevE.57.R2523
(30) Cheng, J.; Potma, E. O.; Xie, X. S., Coherent Anti-Stokes Raman Scattering Correlation Spectroscopy: Probing Dynamical Processes with Chemical Selectivity. *J Phys Chem A* **2002,** *in press*, 8561-8568.
(31) Barbara, A.; Dubois, F.; Quémerais, P.; Eng, L., Non-resonant and non-enhanced Raman Correlation Spectroscopy. *Optics Express* **2013,** *21*, 15418-15418. DOI:10.1364/OE.21.015418
(32) Brokmann, X.; Bawendi, M.; Coolen, L.; Hermier, J.-P., Photon-correlation Fourier spectroscopy. *Optics Express* **2006,** *14*, 6333-6333. DOI:10.1364/OE.14.006333
(33) Marshall, L. F.; Cui, J.; Brokmann, X.; Bawendi, M. G., Extracting spectral dynamics from single chromophores in solution. *Physical Review Letters* **2010,** *105*, 1-4. DOI:10.1103/PhysRevLett.105.053005

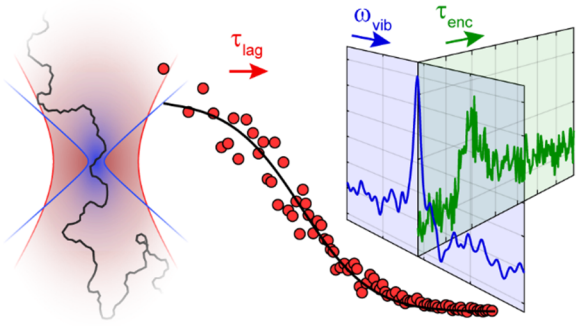




6

# Supporting Information for:

# Fluorescence-Encoded Infrared Vibrational Spectroscopy with Single-Molecule Sensitivity

Lukas Whaley-Mayda[†], Abhirup Guha[†], Samuel B. Penwell[†], and Andrei Tokmakoff[†*]

[†]Department of Chemistry, James Franck Institute, and Institute for Biophysical Dynamics, The University of Chicago, Illinois 60637, United States
[*]Corresponding Author: Email: tokmakoff@uchicago.edu

## Contents

# 1 Sample preparation and steady-state FTIR, UV/Vis absorption, and fluorescence spectra

Coumarin 6 (C6) was used as received from Acros Organics. Solutions for steady-state fluorescence (3 $\mu$M) and UV/vis absorption (40 $\mu$M) measurements were prepared in acetonitrile. For FTIR absorption a 2 mM solution in acetonitrile-d3 was used to take advantage of higher solvent transparency.

The fluorescence emission spectrum was recorded with a Horiba Fluorolog 3 spectrometer using right-angle detection from a 1 cm pathlength cuvette. The UV/vis absorption spectrum was measured at 1 cm pathlength in a Cary 5000 UV-Vis-NIR spectrophotometer. The FTIR spectrum was collected in a Bruker Tensor 27 spectrometer with the solution held in a 500 $\mu$m pathlength demountable cell with Barium Fluoride windows (Spectral Systems). The spectrum in main text Figure 1c is solvent-subtracted.

Solutions used for all FEIR experiments, including the concentration dependence, were prepared in acetonitrile-d3 by serial dilution.

# 2 Experimental details of FEIR instrumentation

The instrumentation used for the FEIR experiments performed here builds on the optical design described previously in Whaley-Mayda *et al*,[1] with the key modification of a new, custom-built microscope used for IR and visible beam delivery and fluorescence detection. The new microscope design allows for higher IR throughput into the sample, simplified alignment and diagnostic capabilities, and higher fluorescence collection efficiency. The generation and characterization of femtosecond mid-IR and visible pulses from the 1 MHz fiber laser pump (Coherent Monaco 1035-40) via a home-built optical parametric amplifier (OPA) and frequency-doubling of the fundamental, respectively, is the same as in ref. 1. Likewise for the Mach-Zehnder interferometer used to produce IR pulse-pairs with controllable delay $\tau_{\mathrm{IR}}$. A second mechanical translation stage (AeroTech ANT95-50L-MP) was added in the visible line to allow for independent control of the $\tau_{\mathrm{enc}}$ and $\tau_{\mathrm{IR}}$ time-delays.

The FEIR microscope, shown schematically in main text Figure 1b, was constructed largely using components from the Thorlabs Cerna Series. The visible objective lens (Zeiss A-Plan 63x NA 0.8) and Zinc Selenide (ZnSe) aspheric lens (ISP Optics ASPH-ZC-25-12, NA$\approx$0.7) used for focusing the visible and IR beams, respectively, are the same as used in ref. 1, and the characterization of their respective focal spots reported therein remains valid. The linearly polarized visible beam is routed through a $\lambda/2$ waveplate (Thorlabs WPH10M-514) to set the polarization relative to the IR beam in the sample (parallel polarization was used exclusively). A dichroic mirror (Semrock FF526-Di01) reflects the visible beam towards the sample and transmits the fluorescence, which is passed through a notch (Thorlabs NF-514-17) and bandpass (Semrock FF01-550/49) filter before being focused by a 150 mm focal length lens (Thorlabs AC254-150-A) onto a single-photon avalanche photodiode (SPAD, MPD PDM 50). This focal length was chosen to produce the magnification required to roughly match the image size of visible focus' airy disk (45.5 $\mu$m) with the active area of the detector (50 $\mu$m), thereby creating confocal conditions. The combined transmission spectrum of the dichroic, notch, and bandapss filters is shown in green in main text Figure 1d.

The estimate of 1% overall fluorescence collection efficiency cited in the main text is calculated by multiplying together estimates of the objective collection efficiency (10%), overlap of emission bandpass and fluorescence spectrum (21%), and detector quantum efficiency (45%).[2] The 10% objective collection efficiency is calculated via $\sin^2(\theta/2)$ for the acceptance half-angle $\theta = \arcsin(\mathrm{NA}/n)$

in acetonitrile ($n = 1.34$).

Sample solutions were held in a home-built cell between a 175 $\mu$m thick glass coverslip (top, visible/fluorescence side) and 1 mm thick Calcium Fluoride ($CaF_2$) window (bottom, IR side) separated by a 50 $\mu$m thick Teflon spacer. The sample is mounted to three axes of translation (Thorlabs PLS-XY and ZFM2020) driven by a Thorlabs MCM3001 controller for positioning into the focus. The onset of thermal effects (described in detail in the SI of ref. 1) caused by the IR absorption of the poorly transparent glass coverslip limits the maximum IR power used in this work (constant in all FEIR experiments at 50 nJ pulse energy, 50 mW average power, 23 kW/cm$^2$ average focal intensity). However, we note that replacing the glass coverslip with a 200 $\mu$m thick $CaF_2$ window removes heating artifacts and allows for at least 50% higher IR powers (the maximum currently available from the OPA).

As described in ref. 1, FEIR data for 1-IR-pulse relaxation transients and Fourier transform spectra is acquired by continuously scanning the relevant delay stage and using a position-tracking waveform (position synchronized output (PSO)) derived from the stage controller (AeroTech A3200 Npaq) to assign photons to their respective delay bins on the fly. A scan speed of 2 mm/s was used for all FEIR measurements, which takes about 3-4 seconds per scan (both directions of travel) for the delay ranges used ($\tau_{\mathrm{enc}}$ over -3 to 10 ps, $\tau_{\mathrm{IR}}$ over -2 to 8 ps for 30 $\mu$M and 30 nM data, and -2 to 6 ps for 1 nM data). For the 30 $\mu$m data in Figures 1e, 1f, and 4d, multiple sans were accumulated over at most 5 minutes and averaged together. For the 1 and 30 nM data in Figures 4c and 4d, scans were accumulated for 30 minutes. The methods for processing time-domain FEIR data into a Fourier transform spectrum are described in ref. 1.

1-IR-pulse scans and the FEIR-CS measurements are performed with the IR pulse-pair set at zero delay ($\tau_{\mathrm{IR}} = 0$). Doing so relies on maintaining inteferometric stability of the relative pathlength between the arms of the Mach-Zehnder interferometer over the course of the measurement. Considering stability at the $\lambda/10$ level for the $\sim$6 $\mu$m mid-IR wavelength used results in the requirement of resilience to pathlength fluctuations and drift on the order of 0.6 $\mu$m, which is readily met in practice.

## 3 Time-gated photon aquisition with TCSPC

Time-correlated single-photon counting (TCSPC) is performed using a PicoQuant Time-Harp 260 PICO PCIe card. The sync channel is provided by a delay generator (SRS DG645) triggered off the fiber laser amplifier. The photon channel is the 15dB attenuated NIM output of the SPAD. For FEIR measurements the PSO waveform from the delay stage controller is sent to the TCSPC card and used as a marker integrated into the time-tagged time-resolved (TTTR) photon record. This raw TTTR record is either processed on the fly by custom LabView code, or saved for analysis in post-processing. The result is two-dimensional data, where one dimension is the scanned optical delay ($\tau_{\mathrm{enc}}$ or $\tau_{\mathrm{IR}}$), and the other is the photon arrival time relative to the sync channel (microtime) with 25 ps bins. The TCSPC instrument response function (IRF) was measured from visible pump light reflected from the air-coverslip interface with the spectrally-selective fluorescence filter-set replaced with appropriate neutral density filters.

Figure S1a shows the raw microtime-resolved count data from a 1-IR-pulse measurement on a 30 $\mu$m C6 solution. Here and in all other 1-IR-pulse scan data in this work the $\tau_{\mathrm{enc}}$ bin size is 40 fs. Figure S1b shows the projection of this raw data onto the $\tau_{\mathrm{enc}}$ axis (i.e. integration over microtime). Figure S1c shows the projection onto the microtime axis, producing a TCSPC histogram. To avoid distorting the microtime decay kinetics the maximum count rate (indicated on the right y-axis of Figure S1b) is kept below 5% of the repetition-rate.[3] The IRF, shown in gray in Figure S1c, has a 250 ps FWHM with a more slowly relaxing tail for positive microtimes. The zero of microtime is set at the maximum of the IRF.

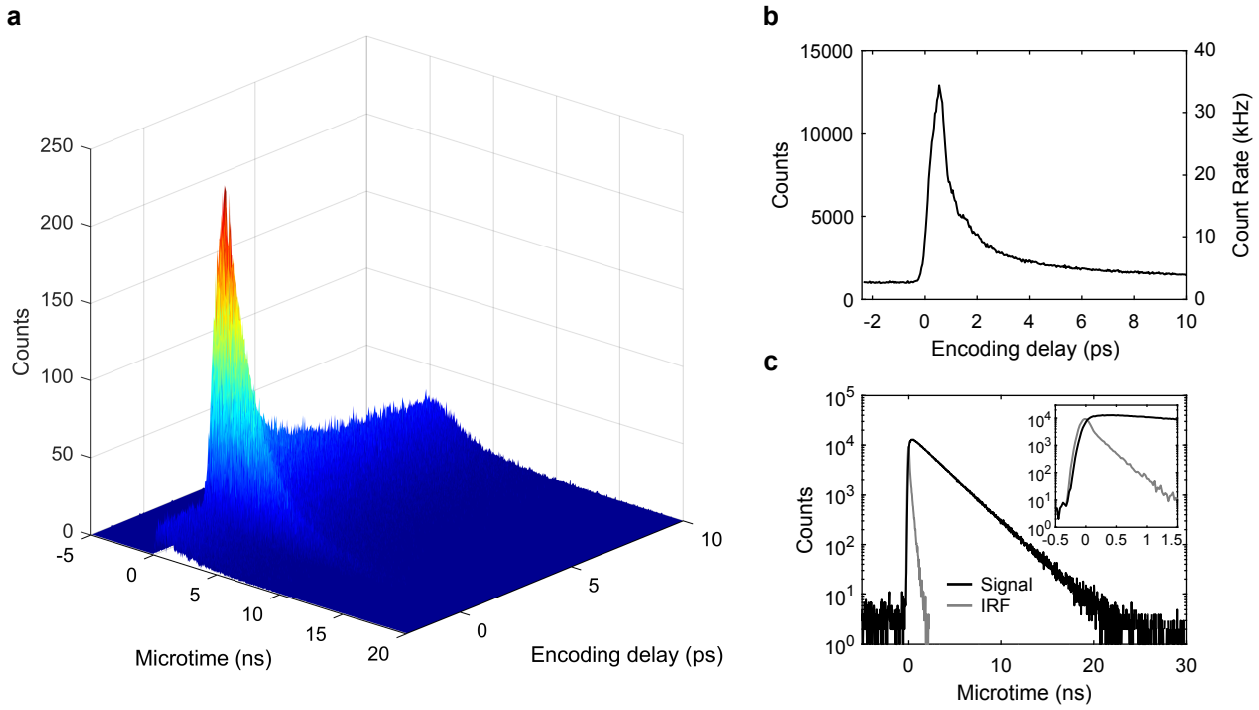


Figure S1: (a) Microtime-resolved photon count data for a 1-IR-pulse FEIR measurement on 30 $\mu$m C6. (b) Projection onto the $\tau_{\mathrm{enc}}$ axis. (c) Projection onto the microtime axis (black), and the IRF (gray). Inset shows detail of the early time data.

As discussed in the main text, we time-gate the photon data based on microtime to remove scattering background. Figure S2a shows TCSPC histograms of every photon's microtime from 1-IR-pulse FEIR measurements on C6 solutions at 30 $\mu$M, 30 nM, and 1 nM, along with the IRF. At the highest concentration the emission kinetics show a clean single-exponential decay with a 2.5 ns lifetime, indicating that the majority of detected photons are C6 fluorescence. At 30 nM a prompt component due to scattering that conforms to the shape of the IRF appears, and by 1 nM dominates the distribution. Due to the separation of timescales between the IRF duration and fluorescence lifetime, a substantial portion of this scattering component can be eliminated by only accepting photons within the time gate indicated by dashed lines in Figure S2a. As shown in Figure S2b, the resulting time-gated 1 nM FEIR transient has a 4-fold reduction in background and subsequently contends with less shot noise than the raw, un-gated data—at the expense of a 30% loss in FEIR signal counts. This gated 1 nM FEIR transient is shown in main text Figure 3c. The dependence of the FEIR signal $F_1$, background $F_0 + B$, and modulation ratio $M = F_1/(F_0 + B)$ on the starting edge of the time gate (Figure S2c) demonstrates this tradeoff between improving signal to background and losing signal, with what we believe to be a roughly optimal compromise at 1 ns indicated. Figures S2d and S2e demonstrate the background-reducing effect of this time-gate on the 1-10 nM range of the C6 concentration dependence (un-gated data same as main text Figure 2). We note that time-gating offers minimal improvement for FEIR spectra, as the Fourier transform filters the background out with the DC component while its associated noise is distributed across the entire frequency axis, diluting its contribution within the IR pulse bandwidth.

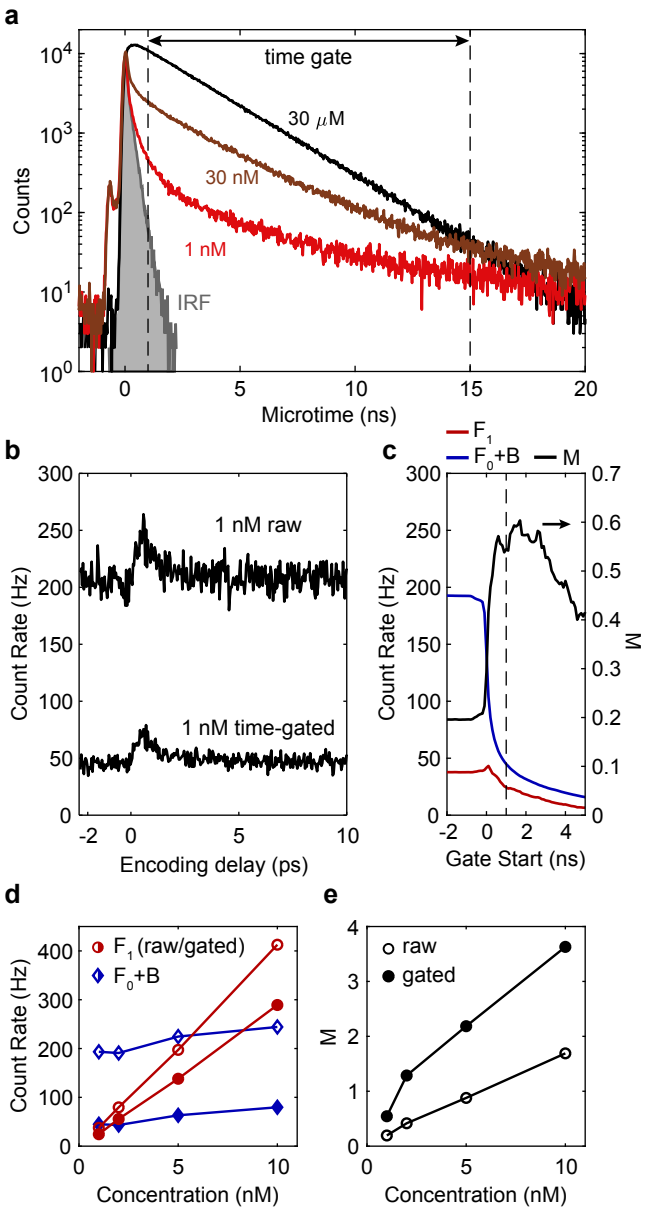


Figure S2: (a) TCSPC histograms from 1-IR-pulse FEIR measurements on C6 at 30 $\mu$M (black), 30 nM (brown), and 1 nM (red) with the IRF (gray). The time-gate (1 ns to 15 ns) used in panels (b), (d), and (e) is indicated by dashed black lines. (b) Comparison of raw and time-gated 1-IR-pulse FEIR measurements at 1 nM. (c) $F_1$ (red) and $F_0+B$ (blue) count rates (left y-axis), and $M$ (black, right y-axis) from the data in panel (b) as a function of the starting edge of the time gate with the ending edge fixed at 15 ns. The optimal starting edge at 1 ns is indicated by a dashed black line. (d) $F_1$ (red circles) and $F_0+B$ (blue diamonds) count rates as a function of C6 concentration. Filled symbols are time-gated, open symbols are raw. (e) Modulation ratios corresponding to the count levels in panel (d). The visible pulse energy used for (b)-(e) and the 1 nM data in (a) was 12 pJ.

# 4 FEIR-CS data aquisition and processing

Raw photon time-series for FEIR-CS measurements are saved as TTTR records, and the correlation function is computed in post-processing by an algorithm described by Wahl *et al.*[4] Time-series are recorded in 3 minute sections, and the resulting correlation functions are averaged together. Each FEIR-CS correlation function in main text Figure 3a was the result of a 60 minute total acquisition time. Prior to autocorrelation, the time-series are time-gated by microtime, which serves the purpose of removing the artifact caused by detector afterpulsing in a addition to reducing scattering background as discussed above.

Figure S3 demonstrates the removal of the afterpulsing artifact using conventional FCS data from a 1 nM rhodamine 6G (R6G) solution in acetonitrile-d3 as an example. R6G is directly resonant with the visible pulse, and the IR beam is not present. Figure S3a shows TCSPC histograms of the fluorescence signal with the IRF for reference. Afterpulses, caused by residual charge-carriers trapped after the primary photo-electron detection event, can be seen as the low-amplitude resurgence of counts after the hardware-fixed 75 ns dead-time. While rare ($< 0.2\%$ probability[2]), their high time-correlation with true photon counts leads to a prominent spike at early times in the correlation function (Figure S3b). If the afterpulsing temporal distribution function is well characterized, this artifact may be suppressed with a filtering algorithm.[5] However, in our case the repetition-rate (1 MHz) is low enough that the afterpulse distribution fully decays before the next excitation pulse arrives, and therefore afterpulses can be explicitly excluded by only accepting photons for correlation that have microtimes shorter than the 75 ns dead-time. As shown in Figure S3b, gating photons in this way removes the afterpulsing spike, providing clean data all the way to the 1 $\mu$s time-resolution limit (inverse of the repetition-rate).

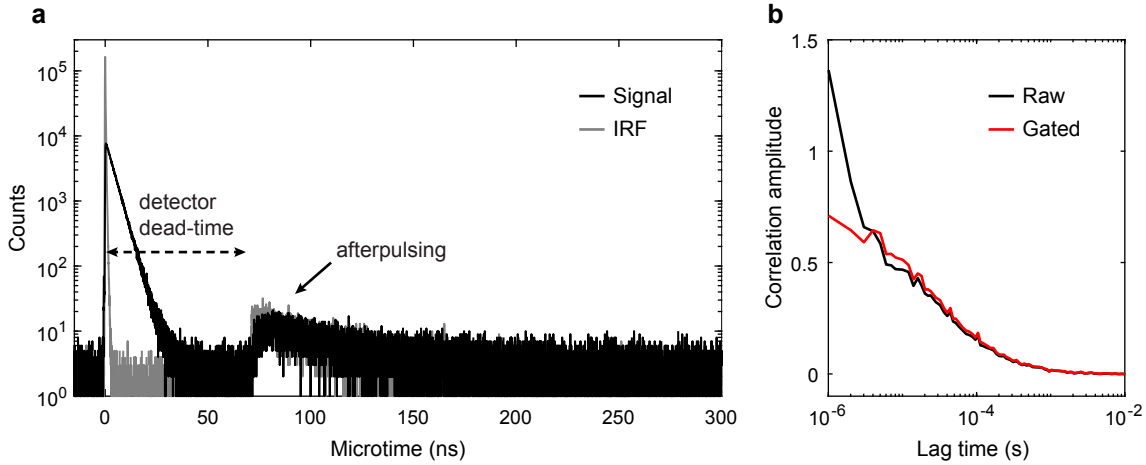


Figure S3: (a) TCSPC histograms of R6G fluorescence and the IRF. The full microtime axis has a range of roughly 819 ns, corresponding to the Time-Harp's $2^{15}$ bins of 25 ps width. (b) FCS correlation functions of the raw time series (all photons, black), and with only accepting photons with microtime $< 30$ ns (excluding afterpulses, red).

The FEIR-CS correlation functions

$$G(t) = \frac{\langle \delta F(0) \delta F(t) \rangle}{\langle F \rangle^2}, \tag{1}$$

where

$$\delta F(t) = F(t) - \langle F \rangle, \tag{2}$$

are fit by the following commonly used model function that assumes diffusion of a single species with diffusion constant $D$ through a 3D ellipsoidal Gaussian probe volume[6]

$$G(t) = \frac{1}{\langle N \rangle} \left( 1 + \frac{t}{\tau_D} \right)^{-1} \left( 1 + \frac{t}{\kappa^2 \tau_D} \right)^{-1/2} \tag{3}$$

with $\tau_D = \frac{w_{xy}^2}{4D}$, $\kappa = \frac{w_z}{w_{xy}}$, and $\langle N \rangle = C\pi^{3/2} w_{xy}^2 w_z$. The average molecule number $\langle N \rangle$ and diffusion timescale $\tau_D$ are fit parameters, and the probe volume aspect ratio $\kappa = \frac{w_z}{w_{xy}}$ (a rather insensitive parameter) is fixed at 4, the value estimated from the visible focal volume characterization in ref. 1. Estimates for the individual probe volume dimensions $w_{xy}$ and $w_z$ can be made based on that characterization, but are not required for the determination of $\langle N \rangle$. While $w_{xy}$ and $w_z$ connect the bulk concentration $C$ to $\langle N \rangle$, the *definition* of $\langle N \rangle$ via the correlation amplitude (i.e. the average occupation number consistent with the Poisson fluctuation statistics) is a conceptually satisfying approach that is independent of the exact shape of the probe volume.

Uncorrelated background contributes to the denominator but not the numerator of $G(t)$ in Eq.1, thereby lowering its amplitude and artificially inflating the measured value of $\langle N \rangle$.[7,8] Reducing the background from scattering by the time-gating method described above is therefore crucial for our FEIR-CS measurements. In general, time-gating or more sophisticated filtering methods using TCSPC can be applied to FCS measurements to improve accuracy or discriminate species by lifetime.[9,10]

Figure S4a shows the effect of varying the starting edge of the time gate on the FEIR-CS correlation function measured from the 1 nM C6 sample (main text Figure 3a). The starting edges relative to the TCSPC histogram are depicted in Figure S4b with the same color-coding. The ending edge of the gate is fixed at 15 ns. As shown in Figure S4c, the early-time correlation amplitude $G(0)$ extracted from the fit increases dramatically as the starting edge is scanned over the prompt scattering component, and appears to reach a saturating value of 1.54 for edges $> 2$ ns. While other background sources with emission kinetics on the fluorescence timescale are likely still present, we take this value, corresponding to $\langle N \rangle = 0.65$ as our best estimate of the average molecule number. As evident in Figure S4a, the signal to noise degrades rapidly for increasingly aggressive time-gates as useful FEIR signal is thrown away, and we choose the 1 - 15 ns gate (cyan curve) as a compromise (used for all correlation functions in main text Figure 3a). The error bars on $\langle N \rangle$ in main text Figure 4b correspond to 95% confidence intervals from the fit routine.

The fit to the 1 nM FEIR-CS correlation function produces a diffusion time constant $\tau_D = 47 \pm 5 \mu$s,

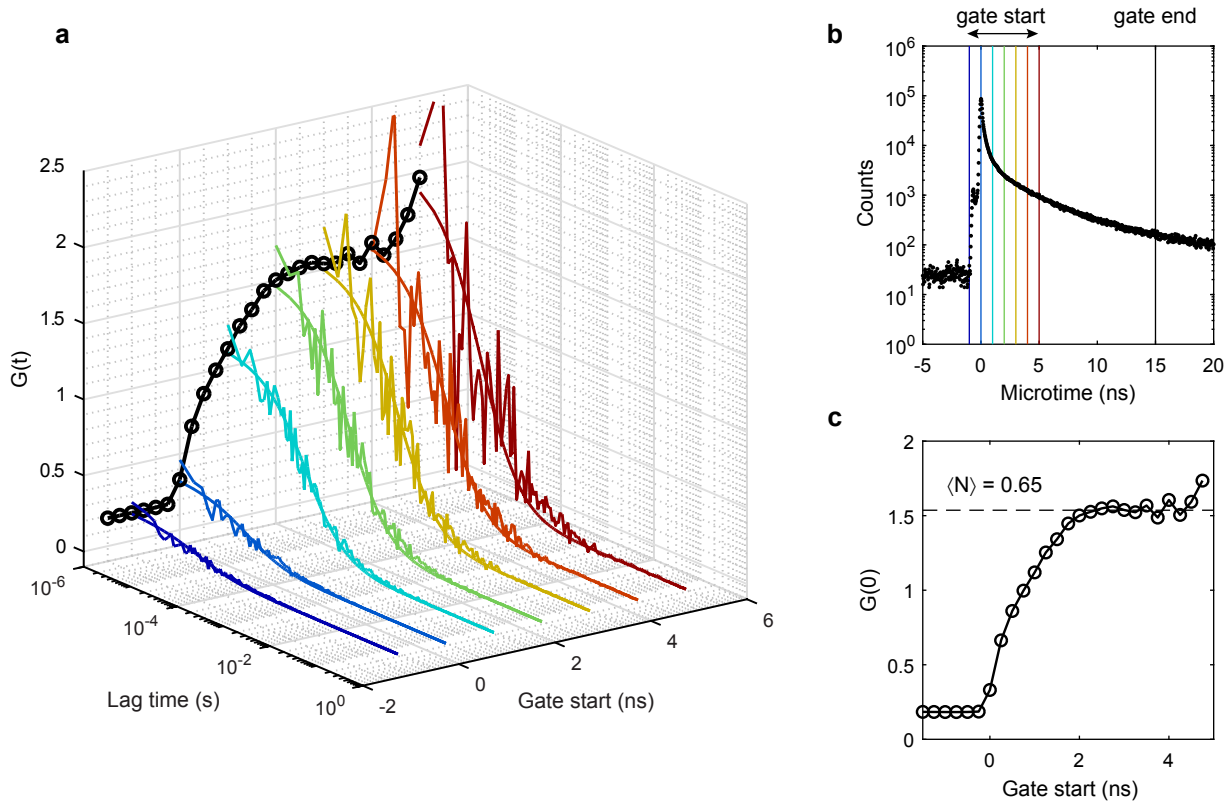


Figure S4: (a) FEIR-CS correlation functions from the 1 nM C6 solution as a function of the time gates displayed in (b). The early-time amplitude $G(0)$ is shown by black circles. (b) Time gates (color-coding matching to (a)) overlaid on the TCSPC histogram. (c) Early-time amplitude $G(0)$ as a function of the starting edge. The saturating value $G(0) = 1.54$ is indicated by a dashed line.

which is longer than that for the conventional FCS measurement on R6G in Figure S3b ($\tau_D = 32 \pm 2\mu$s). Besides differences in molecular diffusion constant, the higher visible power used for the FEIR-CS measurement (26 pJ vs. 1.5 pJ) could result in a slightly larger effective probe volume if saturation effects are at play.[11]

The 110 Hz FEIR count rate per molecule quoted in the main text was determined in part by considering the concentration dependence of the total photon count rate from the time series used for the FEIR-CS measurements, shown in Figure S5. The offset of the linear trend measures the non-molecular background $B$, while the slope of 78 Hz/nM, combined with the determination that $\langle N \rangle = 0.65$ at 1 nM, leads to 120 Hz per molecule ($F_1 + F_0$). Taking into account the $B$-free modulation ratio of 11 implies $F_1 = 110$ Hz. This number is also consistent with the 40 Hz $F_1$ level seen in Figures S2b and c considering that the visible excitation intensity used there is half that for the FEIR-CS measurements (12 pJ vs. 26 pJ).

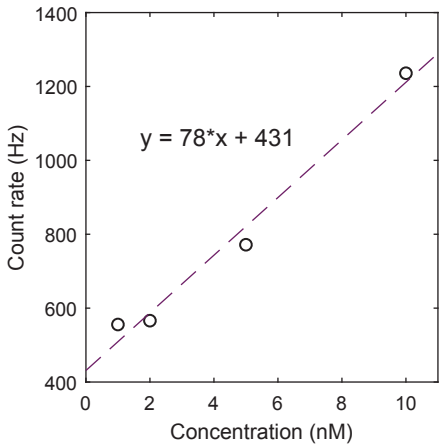


Figure S5: Concentration dependence of the total photon count rate for the time series underlying the FEIR-CS correlation functions (time gated to remove afterpulsing but not scattering). Linear trend shown by dashed line with equation.

## 5 Details of FEIR signal concentration dependence

The maximum FEIR signal $F_1$ and background level $F_0 + B$ shown in the concentration dependence in main text Figure 2a and reproduced here in Figure S6a were extracted from 1-IR-pulse measurements as indicated by the vertical arrows in main text Figure 1e. Time-gating was not used. The count rates were scaled by the variable visible excitation intensity ($I_{\mathrm{vis}}$, average beam power divided by spot size) that was necessary to cover the 5 orders of magnitude in concentration $C$ within the linear range of photon counting detection. The IR intensity was held constant (see Section S2). Implicit in this analysis is the linear dependence of the FEIR signal and one-photon background fluorescence on the visible intensity, which has been verified in ref. 1.

A small deviation from a linear trend (shown as dashed line in Figure S6a) for $F_1$ vs. $C$ is more evident when also dividing through by $C$, which is plotted in Figure S6b. The value of $F_1/(CI_{\mathrm{vis}})$, which should be constant for perfectly linear $F_1$ vs. $C$, decreases by factor of 2 from highest to lowest concentrations. This deviation is most likely due to overestimates of the true concentration in the lower range from accumulated systematic errors in the serial dilution procedure used to prepare the solutions and/or the sticking of dye molecules to interfaces.

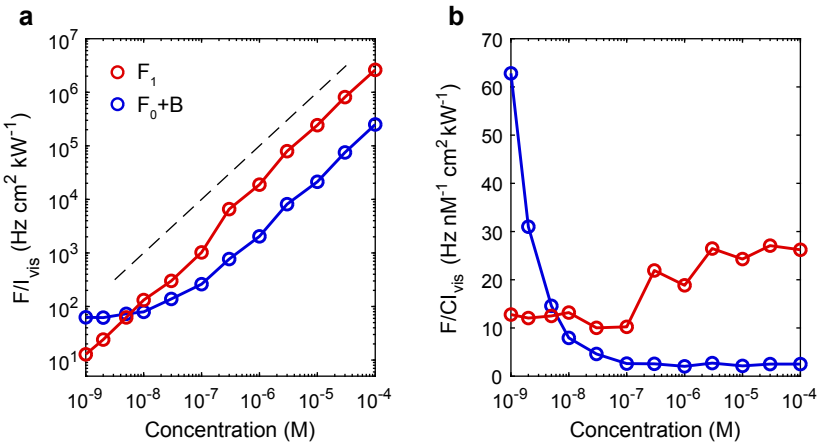


Figure S6: (a) C6 concentration dependence of $F_1/I_{\mathrm{vis}}$ (red circles) and $(F_0 + B)/I_{\mathrm{vis}}$ (blue circles), reproduced from main text Figure 2a. The dashed line shows a linear dependence for reference. (b) Concentration dependence of $F_1/(CI_{\mathrm{vis}})$ (red circles) and $(F_0 + B)/(CI_{\mathrm{vis}})$ (blue circles).

## References


(1) Whaley-Mayda, L.; Penwell, S. B.; Tokmakoff, A. Fluorescence-Encoded Infrared Spectroscopy: Ultrafast Vibrational Spectroscopy on Small Ensembles of Molecules in Solution. *The Journal of Physical Chemistry Letters* **2019**, *10*, 1967–1972, DOI: 10.1021/acs.jpclett.9b00748.

(2) Giudice, A.; Ghioni, M.; Biasi, R.; Zappa, F.; Cova, S.; Maccagnani, P.; Gulinatti, A. High-rate photon counting and picosecond timing with silicon-SPAD based compact detector modules. *Journal of Modern Optics* **2007**, *54*, 225–237, DOI: 10.1080/09500340600763698.

(3) Lakowicz, J., *Principles of Fluorescence Spectroscopy*, 3rd ed.; Springer US: 2006.

(4) Wahl, M.; Gregor, I.; Patting, M.; Enderlein, J. Fast calculation of fluorescence correlation data with asynchronous time-correlated single-photon counting. *Opt. Express* **2003**, *11*, 3583–3591, DOI: 10.1364/OE.11.003583.

(5) Enderlein, J.; Gregor, I. Using fluorescence lifetime for discriminating detector afterpulsing in fluorescence-correlation spectroscopy. *Review of Scientific Instruments* **2005**, *76*, 033102, DOI: 10.1063/1.1863399.

(6) Widengren, J.; Mets, Ü. In *Single Molecule Detection in Solution*, Zander, C., Jorg, E., Keller, R. A., Eds.; Wiley-VCH Verlag GmbH & Co. KGaA: 2003; Chapter 3, pp 69–120.

(7) Koppel, D. E. Statistical accuracy in fluorescence correlation spectroscopy. *Phys. Rev. A* **1974**, *10*, 1938–1945, DOI: 10.1103/PhysRevA.10.1938.

(8) Hess, S. T.; Webb, W. W. Focal Volume Optics and Experimental Artifacts in Confocal Fluorescence Correlation Spectroscopy. *Biophysical Journal* **2002**, *83*, 2300 –2317, DOI: https://doi.org/10.1016/S0006-3495(02)73990-8.

(9) Lamb, D. C.; Schenk, A.; Röcker, C.; Scalfi-Happ, C.; Nienhaus, G. U. Sensitivity Enhancement in Fluorescence Correlation Spectroscopy of Multiple Species Using Time-Gated Detection. *Biophysical Journal* **2000**, *79*, 1129 –1138, DOI: https://doi.org/10.1016/S0006-3495(00)76366-1.

(10) Ghosh, A.; Karedla, N.; Thiele, J. C.; Gregor, I.; Enderlein, J. Fluorescence lifetime correlation spectroscopy: Basics and applications. *Methods* **2018**, *140-141*, Developments in Fluorescence Correlation Spectroscopy and related techniques, 32 –39, DOI: https://doi.org/10.1016/j.ymeth.2018.02.009.

(11) Enderlein, J.; Gregor, I.; Patra, D.; Dertinger, T.; Kaupp, U. B. Performance of Fluorescence Correlation Spectroscopy for Measuring Diffusion and Concentration. *ChemPhysChem* **2005**, *6*, 2324–2336, DOI: https://doi.org/10.1002/cphc.200500414.